Physics Bachelor Research Project

Early Dark Energy and Rayleigh Scattering in the CMB

Author:
Jeffrey Dijkstra
S4468813

Supervisor:
Prof. P. D. Meerburg
Second Supervisor:
Prof. Dr. A. Borschevsky
Daily Supervisor:
Dr. B. Beringue

Faculty of Science and Engineering
University of Groningen
Groningen, the Netherlands
July 2023

Abstract

Early- and late-universe observations of the Hubble constant H_0 show a systematic difference between the two inferred values, termed the Hubble tension. The inclusion of Early Dark Energy (EDE) to the early universe acting as a cosmological constant before quickly decaying away can resolve this tension as it increases H_0 inferred from the cosmic microwave background (CMB). Here is studied the inclusion of Rayleigh scattering to Fisher forecasts of a three parameter EDE extension to the ΛCDM model. Rayleigh scattering is a secondary anisotropy of the CMB caused by the additional scattering of neutral species produced during recombination with a unique frequency dependency ($\propto \nu^4$). EDE Fisher forecasts show benefits when including the Rayleigh signal as it peaks a short time after recombination, tightening constraints on the local expansion history. For this work the Python branch of the Boltzmann hierarchy solver `CAMB` was modified to calculate, for a singe frequency, the total Thomson + Rayleigh power spectrum. The implementation is consistent with the older Fortran Rayleigh branch of `CAMB` to sub-percentile level. The auto RR and cross TR spectra are calculated indirectly from the total spectra which are accurate except for RR at the lowest ℓ. The EDE parameter forecast, including PICO noise levels, give an improvement ranging 54 to 90% (depending on the parameter) for the Rayleigh signal compared to the Thomson primary. This improvement is too high compared to previous studies, particularly $\Omega_c h^2$, H_0 and $f_{\rm EDE}$. The missing cross-correlation terms in the covariance matrices and only including temperature are the possible errors. However, the individual parameter errors are slightly worse than other studies due to excluding polarization effects. Upcoming development in the code, primarily including multi-frequency correlated Rayleigh signals, should clarify whether the forecasts are accurate or correct them to only show minor improvements.

Contents

1 Introduction **3**

2 Theory **4**
2.1 Physics of the Cosmic Microwave Background . . . 4
2.1.1 Power Spectrum . . . 5
2.1.2 Primary anisotropies . . . 7
2.1.3 Secondary anisotropies . . . 7
2.2 Rayleigh Scattering . . . 7
2.2.1 Effects of Rayleigh scattering on the CMB . . . 8
2.3 Early Dark Energy and the Hubble tension . . . 9
2.4 Statistical methods: Fisher forecasts . . . 9

3 Methods: Modeling and Parameter Forecasts **11**
3.1 *Code for Anisotropies in the Microwave Background* (`CAMB`) . . . 11
3.1.1 Old `CAMB` structure . . . 11
3.1.2 New `CAMB` structure . . . 11
3.2 Fisher forecasts and parameter estimation . . . 12
3.3 Noise Modelling . . . 12

4 Results **14**
4.1 Rayleigh effect on power spectra . . . 14
4.2 Fisher forecasts and Early Dark Energy . . . 15

5 Discussion **19**

6 Conclusions **20**

7 References **21**

8 Appendix: Code modifications **23**

1 Introduction

For decades, the Cosmic Microwave Background (CMB) has been one of the most critical foundations of observational cosmology. Its existence provides a source for determining the physical properties of the universe and is a landmark proof of the Big Bang theory. The first observations of the CMB by Arno Penzias and Robert Wilson in 1965 measured an almost uniform blackbody spectrum, while small anisotropies in the temperature and polarization spectrum predicted by cosmological models were later confirmed by the space-based mission COBE [1]. Later missions mapped these primary anisotropies to even higher detail, setting greater constraints on parameters in the standard cosmological model of our universe. These primary fluctuations are expected to come from primordial density perturbations in a plasma consisting of electrons, photons, H and He nuclei. The photons are in equilibrium with electrons by Thomson scattering, the low-energy limit of Compton scattering, such that electrons cannot combine with the nuclei, resulting in a plasma. After the universe expanded outwards sufficiently enough so that the average temperature dropped below a level to sustain this equilibrium, the electrons combined with the nuclei resulting in the universe becoming transparent to photons, seen today as the CMB. Power spectra of the small variations in the CMB temperature and polarization maps show particular features, such as acoustic peaks, providing constraints on the cosmological parameters as varying values result in minute changes in the power spectra.

Over the years, these primary anisotropies have been analysed intensively. However more precise measurements show limitations to the information gained from these cosmic features. Secondary anisotropies previously undetectable are now measurable with next-generation detectors and will help further constrain the cosmological parameters. One such secondary effect is Rayleigh scattering affecting the photon's last scattering surface. After recombination, most electrons will combine with nuclei, causing photons to rarely scatter of electrons. However, the large presence of neutral species after recombination results in a small fraction of photons scattering of these species. This effect leaves a small imprint on the CMB signal and has a signature frequency dependency not shown in Thomson scattering due to the cross section being proportional to $\propto \nu^4$. Models predict the signal peaks some time after the primary signal and quickly decaying away as the universe expands [2]. Moreover, a 4 percent increase in the polarization signal at large scales and high frequencies is expected and is best detectable in the frequency range $200 \leq \nu \leq 800$ GHz [3]. However, the signal's detectability is heavily limited by noise and foregrounds showing a similar frequency dependency. No detection has been achieved at the moment although there is hope it is possible within the next 10 years [4].

Nevertheless, parameter forecasts including Raleigh scattering effects are useful as it can predict possible improvements to the experiment constraining power and aid in the experimental design process. Several codes have been developed that compute the CMB temperature and polarization spectra for a wide range of cosmological models, one being `CAMB`. This code will be used and modified to implement Rayleigh scattering effects to the power spectrum.

One cosmological conundrum that could benefit from including Raleigh effects in the power spectra is the Hubble tension. For several years studies determining the Hubble constant H_0 from early time probes like the CMB systematically give a lower value than studies using local measurements from for example Type Ia supernovae [5]. This inconsistency in H_0 has not yet been solved and is not expected to originate from measurements systematics thus giving rise to proposals that include new physics. One such exotic hypothesis is Early Dark Energy (EDE) which theorizes a new early universe component acting as a cosmological constant, increasing H_0 determined from the CMB before quickly decaying away at some critical redshift. Due to the late time probing of Rayleigh scattering on the CMB power spectra, inclusion of Rayleigh in the EDE parameter forecasts can possibly increase the constraining power. Earlier studies have shown that constraints on both the expansion history as well as the physical densities can benefit from Rayleigh scattering [2], [6], [7]. For that reason, we expect that constraints on EDE could equally benefit from Rayleigh effects.

2 Theory

2.1 Physics of the Cosmic Microwave Background

A short time after the big bang the universe contained three main components: matter, radiation and dark energy with radiation dominating the energy density at this early time. The radiation, consisting of photons and neutrinos, was in thermal equilibrium with the matter component, made of the usual elementary particles but also dark matter. This resulted in a photon-baryon fluid/plasma where the photons are energetic enough to ionize the baryons causing a coupling to the matter component, consisting mainly of hydrogen and helium. The free stream of electrons resulting from this equilibrium causes an opaque universe as Thomson scattering between photons and electrons result in both particles having a low mean free path.

Meanwhile, the combined matter and radiation energy densities drive the universe to expand as described by the Friedmann equations [1]. This expansion stretches particle wavelengths, decreasing the temperature by a factor of $(1 + z)$ with z the redshift. After the universe cooled sufficiently atoms, predominately hydrogen, began to form in a process called *recombination* as the average photon energy decreased far below the ionization energy. Numerically, it is defined as the instant where the number density of ions is equal to the neutral atoms [1]. Afterwards, *decoupling* is defined as the instant the rate of Thomson scattering events became smaller than the Hubble parameter (describing the universes expansion at that instant) causing photons to stop interacting with electrons resulting in a transparent universe. Lastly, the epoch of *last scattering* is the moment an average photon underwent its last scattering of an electron. Hence surrounding every observer there is a last scattering surface from which photons stream freely. This is the moment where density perturbations in the plasma are transferred to the temperature and polarization anisotropies of the released CMB photons. Decoupling and last scattering follow each other closely as a photon is unlikely to scatter once the universe expansion rate is greater than the Thomson scattering rate [1].

The thermal equilibrium between the radiation and matter components results in the energy density of the released photons to be described by a blackbody spectrum over the whole sky. However this observation is contradicted by the causal horizon setting limits on how far information travelled (moving with speed c) since the big bang. Meanwhile, the CMB is uniform on scales larger than this horizon scale causing the horizon problem. Cosmic inflation provides a solution as it describes an early universe the size of the Planck length and its contents in thermal equilibrium and causal connection [8]. The framework of this universe is modeled by the Friedmann-Robertson-Walker (FRW) metric describing a homogeneous and isotropic universe on large scales. On these small scales quantum fluctuations are the primary source of density perturbations of the matter and radiation components. These tiny fluctuations are then projected onto greater scales as inflation causes the universe to rapidly expand disconnecting patches formally in causal contact. After inflation stops and the expansion slows down the horizon grows and the universe becomes homogeneous on large scales with almost scale-invariant inhomogeneities on top. For a detailed introduction to inflation, see [9].

The perturbations in the photon-baryon fluid can be described in terms of the curvature perturbations $\mathcal{R}$ measuring the spatial curvature of a part of the comoving space-time slicing. The power spectrum of the curvature perturbations can be described as a power law [10]:

$$\Delta^2_{\mathcal{R}}(k) = \Delta^2_{\mathcal{R}}(k_*) \left[\frac{k}{k_*}\right]^{n_s-1} = A_s \left[\frac{k}{k_*}\right]^{n_s-1}, \tag{1}$$

with k_* some arbitrary chosen pivot scale, most often the statistical center of the data [5]. For CMB anisotropies the Planck collaboration sets $k_* = 0.05\ \mathrm{Mpc}^{-1}$ [11] which we also adopt here. A_s is the scalar amplitude of the matter power spectrum and n_s the primordial spectral index of the scalar fluctuations which inflation expects to be $n_s \sim 1$ producing a nearly scale-invariant spectrum [12]. The perturbations in the energy density cause gravitational instabilities manifested as potential wells and hills. The photon-

baryon fluid oscillate in this perturbed potential changing the distribution of the fluid which again alters the gravitational field. As mentioned earlier, at decoupling the horizon had a finite scale of around 1° [8]. Thus before last scattering at scales smaller than the horizon, the fluid had time to compress. On even smaller scales the compression continues until radiation pressure resist the fluid movement, halting it, and then expands it again causing acoustic oscillations. The resulting acoustic peaks in the power spectrum are described further in section 2.1.2.

Besides temperature anisotropies the CMB also contains a linear polarization signal, mainly curl-free E and divergence-free B modes. These modes are harder to detect than the T signal. Nonetheless, the E modes almost have been fully mapped with the B modes to be expected in future experiments. Both these modes contain new information that are expected to help studies to fundamental physics [8]. The E-mode is sourced by scattering of the quadrupole temperature anisotropy present around recombination even when the radiation itself is unpolarized [2]. The B modes are sourced by quadrupoles induced by gravitational-waves at recombination, which themself are sourced by the inflation tensor perturbations [13].

The previous described properties of our universe are reasonable explained by the standard cosmological model (or ΛCDM model) describing a universe containing three main components: a cosmological constant (Λ), cold dark matter and ordinary matter. It assumes a spatially flat universe and the density parameters summing to unity [5]. The simplest ΛCDM model contains six independent parameters (listed in Table 1) giving a reasonable fit to the latest observations, though extra parameters can be added to consider more complex models. The parameters cannot be determined individually as significant degeneracies are present in the CMB data. Often assumptions (priors) have to be made to constrain particular parameters [8].

2.1.1 Power Spectrum

To quantify the properties of the CMB, the density anisotropies are converted to a power spectrum giving a measure of the fluctuations over the angular scales. For this the CMB temperature observations can be expanded around a mean $\overline{T}$, along a direction $\hat{\mathbf{n}}$ as $T(\hat{\mathbf{n}}) = \overline{T}(1+\Theta(\hat{\mathbf{n}}))$, with $\Theta(\hat{\mathbf{n}}) \equiv \frac{\delta T(\hat{\mathbf{n}})}{T}$ the fractional temperature fluctuation [10]. Since the CMB anisotropies are described on the last scattering surface of a sphere it is useful to express these fluctuations as a harmonic function expansion [1]:

$$\Theta(\hat{\mathbf{n}}) = \sum_{\ell=0}^{\infty} \sum_{m=-\ell}^{\ell} a_{\ell m} Y_{\ell m}(\hat{\mathbf{n}}), \tag{2}$$

with $a_{\ell m}$ the multipole moments and $Y_{\ell m}(\hat{\mathbf{n}})$ the spherical harmonic functions. Here the multipole ℓ roughly corresponds to the angular scale by $\theta \sim \pi/\ell$ [1]. Because theories cannot predict the exact anisotropies, cosmologist are mainly interested in the statistical properties of this field [12]. One such property of interest is the correlation function between two directions $\hat{\mathbf{n}}$ and $\hat{\mathbf{n}}'$:

$$C(\theta) = \langle \Theta(\hat{\mathbf{n}})\Theta(\hat{\mathbf{n}}')\rangle, \tag{3}$$

where $\cos(\theta) = \hat{\mathbf{n}}\cdot\hat{\mathbf{n}}'$ is the angle between the two directions and $\langle\cdot\rangle$ is the average over multiple realisations of our universe [12]. The rotational invariance due to the isotropic sky means that the multipole correlator function can be written as [12]:

$$\langle a_{\ell m} a^*_{\ell' m'}\rangle = C_\ell \delta_{\ell m}\delta_{\ell' m'} \ , \tag{4}$$

where C_ℓ is the angular power spectrum and thus related to the correlation function. The correlation function in real space is related to C_l by [1]:

$$C(\theta) = \sum_{\ell} \frac{2\ell+1}{4\pi} C_\ell P_\ell(\cos\theta), \tag{5}$$

with P_ℓ the Legendre polynomials. The angular power spectrum for the relevant CMB modes is defined as [2]:

$$C_l^{XY} = \langle a_{lm}^X a_{lm}^Y \rangle, \tag{6}$$

where X and Y can be T or E modes (the B modes sourced by gravitational lensing and tensor fluctuations are not affected by Rayleigh scattering and thus not considered here). Averaging this power function over all m moments (ranging from -ℓ to ℓ) at each ℓ gives $(2\ell+1)C_\ell/4\pi$ [13]. Note that the power spectrum is often portrayed as $D_\ell = \ell(\ell+1)C_\ell/2\pi$ as this gets constant at low ℓ for a scale-invariant curvature spectrum. If the temperature and polarization fluctuations are Gaussian this quantity fully characterizes the anisotropies in the CMB map and is used to deduce the cosmological parameters [13]. The measurements of the CMB temperature power spectrum for various experiments is shown in Figure 1. Here the monopole ($\ell = 0$) of the CMB is the mean temperature $\overline{T} = 2.7255 \pm 0.0006$ K [13]. All CMB

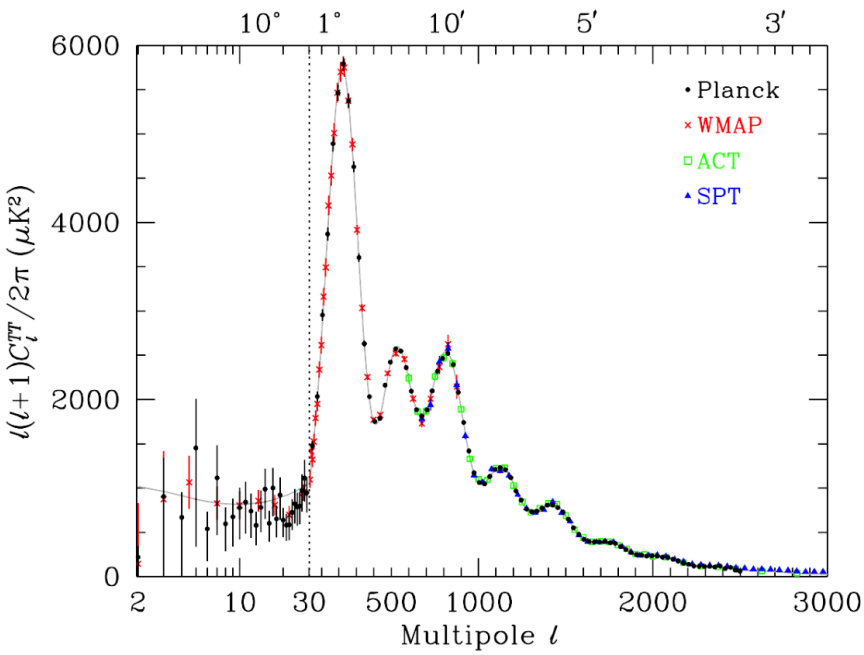

Figure 1: CMB temperature power spectrum measurements from the Planck, WMAP, ACT and SPT missions. Figure taken from Workman et al. [13].

mapping experiments, except COBE, are insensitive to the monopole as they measure only temperature and polarization differences. Meanwhile, the dipole ($\ell = 1$) is the greatest anisotropy and is caused by the motion of the solar system relative to the isotropic CMB [13]. This term is always removed out of the final CMB map. The higher order multipoles ($\ell \geq 2$) are due to the density perturbations present at the last scattering surface of the CMB photons.

The high error at low ℓ (large angular scale) is due to cosmic variance. In earlier equations we averaged over the ensemble of universe realisations. However, only our visible universe is observable to us introducing an intrinsic error to every measurement we make of the cosmological properties. As said earlier, to deduce the underlying distribution function we take the average over all $(2\ell+1)$ multipoles. It can be shown that this estimate of the power spectrum has a cosmic variance of $[2/(2\ell+1)]C_\ell^2$ at each measured C_ℓ [10]. So at low ℓ, few independent modes are available to average over causing the high cosmic variance. Meanwhile at high ℓ the cosmic variance is minor and dominated by other errors such as instrumental noise, resolution and foregrounds [12].

2.1.2 Primary anisotropies

The temperature and polarization anisotropies we observe today are well modelled by probing a background FRW universe with linear perturbations whose evolution is affected by the cosmological parameters. To see how these affect the power spectra we go over the TT auto spectrum (see Figure 1). The particular shape of this spectrum is affected by the cosmological parameters and used to determine their exact values. Starting at low ℓ the power spectrum start on a long plateau as the perturbations did not have enough time to evolve to such large angular scales. The Hubble radius, representing the maximal comoving distance a particle could have travelled, at last scattering is around $\ell \approx 100$, causing lower ℓ to reflect the initial conditions [13]. As the temperature fluctuations originate from variations in the gravitational potential, which is termed the Sachs-Wolfe effect, the gravitational fluctuations at these low ℓ were constant. This is called the Sachs-Wolfe plateau [1].

At larger ℓ the spectrum rises to a series of peaks termed the *acoustic peaks*. These are due to gravitational acoustic oscillations in the baryon-photon plasma before recombination as stated earlier. The perturbations oscillate in potential wells generated primarily by the dark matter component. Here the photon pressure acts as a restoring force and baryon mass as a inertia component. These perturbations are sufficiently small in amplitude to be treated as linear so that the system is described as a driven harmonic oscillator with the spatial frequency related to the sound speed in the fluid [13]. The oscillations in the fluid gives rise to temperature fluctuations which at last scattering freeze in the temperature map seen today as a series of harmonic peaks. The first and next odd peaks represent the modes that compressed maximally before recombination while the even peaks are the maximum under-density rarefaction's. The even peaks are generally smaller in amplitude as the fluid's inertia holds back the rebound [10].

At further increasing ℓ there is a damping tail that is caused by the last scattering surface having a depth as recombination does not happen instantaneously. Fluctuations at angular scales smaller then this depth are damped as the photons make random walks in the fluid during recombination mixing the hot and cold patches. This causes the acoustic oscillations on scales smaller than the random walk to decay over time and is responsible for why C_ℓ's at even higher ℓ are harder to measure [13].

2.1.3 Secondary anisotropies

Besides primary anisotropies, secondary effects happening after recombination can leave imprints on the CMB. One effect is parameterized by the reionization optical depth τ with the optical depth being the probability that a photon scatters once assuming the reionization happens instantaneous and completely [5]. Here reionization refers to the period when the first stars were born and ionized the baryonic matter. Thus CMB photons scatter again of free electrons, although much less frequently than before recombination as the expansion of the universe diffused matter significantly. The universe has remained transparent to this day with a low density of ionized hydrogen and helium. Nevertheless, these few scattering events leave a small imprint on the CMB which must be taken into consideration when examining the power spectra. While reionization is not instantaneous, τ is still a useful measure of the mean redshift of the event [5].

In addition, the gravitational bending of CMB photons, called lensing, from compact objects in the later universe distorts the temperature and polarization anisotropies at high ℓ. Apart from being an effect that must be considered when modelling the CMB, lensing can also help constrain certain parameters from the power spectra. Most notably the neutrino masses and dark-energy evolution [13].

Rayleigh scattering can also be considered a secondary anisotropy which will be the topic of this thesis and discussed in the next section.

2.2 Rayleigh Scattering

Rayleigh scattering is the scattering of photons from neutral species with the particle size much smaller than the photon wavelength. The cross section is given by [3], [6]:

$$\sigma_R(\nu) \;=\; \sigma_T \left[\sum_{j=2}^{\infty} f_{1j} \frac{\nu^2}{\nu_{1j}^2 - \nu^2} \right]^2 , \tag{7}$$

with ν_{1j} and f_{1j} the Lyman series frequencies and oscillator strengths respectively and $\sigma_T = \frac{8\pi}{3}\left(\frac{q^2}{4\pi\epsilon_0 mc^2}\right)^2$ the Thomson scattering cross section. The Lyman series frequencies are of order 3 PHz, while the photon frequencies at recombination are many orders of magnitude smaller making it possible to Taylor expand the expression [6]. By defining $\nu_{\text{eff}} = \sqrt{8/9} R_\infty c \approx 3.102 \cdot 10^6$ GHz ≈ 12.83 eV with R_∞ the Rydberg constant, equation (7) can be approximated as:

$$\sigma_R(\nu) \;\approx\; \sigma_T \left[\left(\frac{\nu}{\nu_{\text{eff}}}\right)^4 + \alpha \left(\frac{\nu}{\nu_{\text{eff}}}\right)^6 + \beta \left(\frac{\nu}{\nu_{\text{eff}}}\right)^8 + \; ... \right] , \tag{8}$$

with $\alpha \approx 2.626$ and $\beta \approx 5.502$ [3]. For frequencies well below ν_{eff} the Rayleigh scattering cross section is therefore described by a $\propto \nu^4$ dependency in contrast to the frequency independent Thomson scattering.

2.2.1 Effects of Rayleigh scattering on the CMB

Rayleigh scattering changes the comoving opacity in the recombination history from [6]

$$\dot{\tau} = a n_e \sigma_T ,$$

to

$$\rightarrow \dot{\tau}(\nu) = a n_e \sigma_T + a(n_{\text{H}} + R_{\text{He}} n_{\text{He}}) \sigma_R(\nu). \tag{9}$$

Here, $R_{\text{He}} \approx 0.1$ accounts for the relative strength of Rayleigh scattering for Helium atoms compared to Hydrogen [3]. The visibility function is defined as [10]:

$$g(z) = \dot{\tau} e^{-\tau}, \tag{10}$$

with τ the optical depth. It is the probability density that a photon last scattered at a particular redshift. Thus the visibility function becomes frequency dependent due to the altered comoving opacity. Moreover, the increased total coupling between photons and baryons shifts the last scattering surface and consequently the visibility function to later times [2].

As stated earlier, the photon mean free path in the plasma controls the strength of diffusion damping. Including Rayleigh scattering will reduce the mean free path as there is an increased probability of photons scattering. So Rayleigh reduces the amplitude of diffusion damping. However, this only holds at low frequencies. At higher frequencies, the visibility function is shifted to later times where the mean free path is overall longer leading to an increase in the damping [2]. Moreover, the last scattering surface gets frequency dependent causing the size of the sound horizon at last scattering to also become frequency dependent showing an increase at higher frequencies. The increase shifts the acoustic peaks in the CMB and matter power spectra to smaller ℓ [2]. Lastly, Rayleigh scattering also produces polarization modes as the scattering structure from the induced dipoles in the classical limit is the same as in Thomson scattering and so can be handled the same way in the Boltzmann code [3]. The shift in the visibility function increases these local temperature quadruples around recombination resulting in a boost to polarization E modes at small ℓ [2]. In theory B modes would also be affected by Rayleigh scattering but because the polarization originates from a wide scale range where Rayleigh has a varying sign, the contribution to the lensed BB spectrum partially averages out [3].

2.3 Early Dark Energy and the Hubble tension

Since the first estimate by Edwin Hubble, the Hubble constant has been under heavy discussion by scientists and many missions undertaken to pin down its value. Two main ways exist to infer H_0: determine it from early time probes as is done most recently by the Planck Collaboration giving a value $H_0 = 67.4 \pm 0.5$ km s^{-1} Mpc^{-1} [11]. The second are local measurements using a variety of astronomical sources such as: Type Ia supernovae acting as calibrated cosmic distance ladders, time delays in gravitationally-lensed quasars and most recently gravitational waves from standard sirens such as the binary neutron star GW170817 [5]. All these methods give a higher H_0 value. For example, the SH0ES team using Cepheid variables reports a baseline $H_0 = 73.04 \pm 1.04$ km s^{-1} Mpc^{-1} [14], and overall disagree at a $\gtrsim 5\sigma$ level with values from CMB experiments [5], [15]. This conflict of H_0 between local measurements and a ΛCDM fit to the CMB is termed the Hubble tension. Possible measurement and calibration systematics in either the local or CMB methods cannot easily explain this difference and therefore attention is given to possible hints of new physics [16].

Several resolutions to the Hubble tension have been proposed but many are heavily constrained by the acoustic peaks in the CMB power spectrum [16]. One exotic solution that is less constrained includes an early time ($z \gtrsim 3000$) dark energy component termed Early Dark Energy (EDE). Many physical models of EDE have been proposed including an oscillating scalar field ϕ which we will focus on in this thesis. Here a scalar field at early times is displaced from its potential minimum and frozen, acting as a cosmological constant. However, when the Hubble parameter drops below the mass of the field at some critical redshift z_c, the field falls back to the potential minimum oscillating around it resulting in a decay of its contribution to the energy density. The field now behaves as a fluid decaying similar or faster than the radiation component. This increases the early expansion of the universe while leaving the later evolution unaltered resulting in a reduced sound horizon at decoupling giving a higher H_0 from the CMB [16]. The model is described in terms of: $f_{\rm EDE}(z_c) \equiv \Omega_\varphi(z_c)/\Omega_{tot}(z_c)$ being the maximal EDE energy density fraction of the universe, z_c the redshift at which $f_{\rm EDE}$ is a maximum and $\theta_i \equiv \phi_i/f$ the initial field displacement [17]. z_c roughly corresponds to the moment just before oscillations occur.

Although current data cannot confirm the existence of EDE, it remains one of the prime candidates to resolve the Hubble tension and future experiments are expected to decisively establish whether EDE should be incorporated into current cosmological models [18]. In this thesis, Rayleigh effects are considered in the EDE parameter forecasts as the late time recombination sampling inherent to Rayleigh scattering can possibly help establish the parameters of EDE.

2.4 Statistical methods: Fisher forecasts

A statistical tool that can access the parameter constraining power of future CMB experiments is a Fisher forecast. This tool is useful as it can test the detectability of Rayleigh scattering before actual measurements and thus is instrumental for experimental designs and forecasts of parameter errors. The technique assumes that the likelihood is Gaussian around its maximum which may not represent the true likelihood. Nevertheless, the likelihood can still be approximated to be locally Gaussian around the maximum making this technique viable for a wide range of cases [19]. Assuming a noiseless survey, the likelihood $\mathcal{L}(\theta|\boldsymbol{d})$ with θ a vector of cosmological parameters and $\boldsymbol{d}$ the data vector is [2]:

$$\mathcal{L}(\theta|\boldsymbol{d})) \propto \frac{1}{\sqrt{\det(\mathbf{C}(\theta))}} \exp\left(-\frac{1}{2}\mathbf{d}^\dagger(\mathbf{C}(\theta))^{-1}\mathbf{d}\right), \tag{11}$$

where $\mathbf{C}(\theta)$ is the theoretical covariance. The Fisher matrix is defined as [19]:

$$F_{ij} = -\left\langle \frac{\partial^2 \ln \mathcal{L}}{\partial\theta_i\theta_j} \right\rangle, \tag{12}$$

where $\langle\cdot\rangle$ is again the ensemble average over the observational data. It originates from Taylor expanding the log likelihood surface and contains the parameter errors and covariance. Because the likelihood of

independent data sets is the product of the likelihoods, the Fisher matrix of the independent data sets is the sum of each Fisher matrix. This allows not only for easy implementation of noise to the Fisher matrix but also merging several suitable data sets to increase the constraining power. From the Fisher matrix it can be shown that the standard deviation in a parameter estimation is given by [19]:

$$\sigma_{ij}^2 \geq \left(F^{-1}\right)_{ij}, \tag{13}$$

and when estimated simultaneously for all parameters the marginalized error is:

$$\sigma_{\theta_i} \geq \left(F^{-1}\right)_{ii}^{1/2}. \tag{14}$$

This inequality is the Cramér–Rao bound and is the best case estimate possible of the errors due to not only excluding systematics and real world errors in the Fisher matrix but also, fundamentally, when approximating the likelihood to be Gaussian [19]. When combining equations (11) and (12) the Fisher matrix for CMB experiments is [2]:

$$F_{ij,\ell} = \frac{1}{2}\mathrm{Tr}\left[(\boldsymbol{C}_\ell)^{-1}\,\frac{\partial \boldsymbol{C}_\ell}{\partial \theta_i}\,(\boldsymbol{C}_\ell)^{-1}\,\frac{\partial \boldsymbol{C}_\ell}{\partial \theta_j}\right], \tag{15}$$

where each ℓ corresponds to $f_{sky}(2\ell+1)$ independent modes. Thus the total Fisher matrix is:

$$F_{ij} = \sum_\ell f_{sky}(2\ell+1)F_{ij,\ell}. \tag{16}$$

The covariance matrix normally used when including Rayleigh effects to the power spectra for estimating the parameter constraints is [2]:

$$\boldsymbol{C}_\ell^{\nu\nu} = \begin{pmatrix} \boldsymbol{C}_\ell^{TT} & \boldsymbol{C}_\ell^{TR} \\ \boldsymbol{C}_\ell^{TR} & \boldsymbol{C}_\ell^{RR} \end{pmatrix}. \tag{17}$$

Here $\mathbf{C}_\ell^{TT}$, $\mathbf{C}_\ell^{TR}$ and $\mathbf{C}_\ell^{RR}$ are the $N_\nu \times N_\nu$ frequency covariance matrices of the Thomson auto, Thomson-Raleigh cross and Rayleigh auto power spectra respectively. This way all frequency auto- and cross spectra are accounted for. Noise can be easily implemented by adding noise power spectra $\mathbf{N}_\ell$, which are $N_\nu \times N_\nu$ diagonal frequency matrices, to the diagonal elements [2]. However, the code used in this thesis can only calculate single-frequency Rayleigh spectra. To circumvent this a low-frequency map will be cross-correlated with a high-frequency map leading to partially uncorrelated Thomson and Rayleigh signals. To approximate this the covariance matrix will consist of a primary Thomson + low ν Rayleigh signal in the (0,0) element and a primary Thomson + high ν Rayleigh signal in the (1,1) element. The off-diagonal elements contain the Thomson primary and two TR spectra at low and high ν. The described Rayleigh covariance matrix is:

$$\mathbf{C}_\ell^{\nu_1\nu_2} = \begin{bmatrix} C_\ell^{TT} + 2\left(\frac{\nu_1}{500}\right)^4 C_\ell^{TR} + \left(\frac{\nu_1}{500}\right)^8 C_\ell^{RR} + N_\ell(\nu_1) & C_\ell^{TT} + \left(\frac{\nu_1}{500}\right)^4 C_\ell^{TR} + \left(\frac{\nu_2}{500}\right)^4 C_\ell^{TR} \\ C_\ell^{TT} + \left(\frac{\nu_1}{500}\right)^4 C_\ell^{TR} + \left(\frac{\nu_2}{500}\right)^4 C_\ell^{TR} & C_\ell^{TT} + 2\left(\frac{\nu_2}{500}\right)^4 C_\ell^{TR} + \left(\frac{\nu_2}{500}\right)^8 C_\ell^{RR} + N_\ell(\nu_2) \end{bmatrix}. \tag{18}$$

However, cross-correlating the low and high ν maps also needs the $C_\ell^{RR}(\nu_1 \times \nu_2)$ term in the off-diagonal elements. This term cannot be outputted by our version of the code at this point. For the Thomson primary forecast the previous covariance matrix is used without the Rayleigh terms giving:

$$\mathbf{C}_\ell^{\nu_1\nu_2} = \begin{bmatrix} C_\ell^{TT} + N_\ell(\nu_1) & C_\ell^{TT} \\ C_\ell^{TT} & C_\ell^{TT} + N_\ell(\nu_2) \end{bmatrix}. \tag{19}$$

In these two matrices, $N_\ell(\nu)$ is the PICO noise power spectrum described further in section 3.3.

3 Methods: Modeling and Parameter Forecasts

Modelling inhomogeneities in the primordial photon density is complex as the photons are connected to other components present in the plasma. Photons are affected by gravity and the free electron distribution, through Thomson scattering, which itself is tightly coupled to the nuclei and gravity. Additionally, the metric, describing the geometry and causal structure of spacetime, is influenced by all aforementioned including dark matter. To solve the photon distribution thus requires solving the distribution for all these components using the Boltzmann equations that tracks the photon distribution function evolution. The Boltzmann hierarchy provides a framework for a quick numerical solver of the Boltzmann equations. For a deeper overview of this framework see [12].

3.1 *Code for Anisotropies in the Microwave Background* (`CAMB`)

Several codes exist that solve the Bultmann equations and hierarchy numerically, one being `CAMB` created by A. Lewis and A. Challinor in the early 2000s [20]. It is based on `CMBFAST` developed by U. Seljak and M. Zaldarriaga and was originally fully written in Fortran 90 although new versions have released that include a Python wrapper. `CAMB` can, when giving a set of cosmological parameters and model universe, compute the temperature and polarization auto and cross correlation power spectra. Additionally, it can compute the transfer and backgrounds functions and the matter power spectrum. Besides the standard recombination calculator the Fortran codes include a Rayleigh branch computing the effects of Rayleigh scattering on the power spectrum. However, the new `CAMB` Python version misses this function. By comparing how Rayleigh is implemented in old `CAMB`, the feature will be added to the new version of `CAMB`. To understand the differences between the two codes and how `CAMB` calculates the power spectra a review of each code structure will be provided below.

3.1.1 Old `CAMB` structure

The code starts with params.ini specifying the necessary cosmological parameters including extra terms that are required for different model universes. For example, setting the various mass fractions, enabling reionization, choosing which polarization and scalar/vector/tensor modes can all be tweaked. The Rayleigh branch includes an option specifying which frequencies are used in the computations. Additionally, in params.ini the working and accuracy of the code is specified by several accuracy parameters. However, increasing the accuracy of `CAMB` comes with a significant time penalty in the calculations. Next the file inidriver.f90 reads params.ini and prompts the code to run.

The other .f90 files can be divided into two main categories: utilities and cosmology. The utilities such as bessel.f90 and utils.f90 support the cosmology code with various miscellaneous tasks while the cosmology files fulfill the main computations and are divided into subtasks such as reionization.f90 and lensing.f90 performing the reionization and CMB lensing calculations respectively. Each file uses modules which are either defined itself in the code or are used from other files. After the calculations, `CAMB` gives the output in several files containing the lensed, unlensed and scalar or tensor modes. The C_ℓ's are given in terms of $D_\ell = \ell(\ell+1)C_\ell/2\pi$ in units $\mu\mathrm{K}^2$.[1]

3.1.2 New `CAMB` structure

The python wrapper of `CAMB` offers the possibility to run the code from a python script editor with the various parameters now accessed and edited through a series of function that call the `CAMB` subroutines. Meanwhile the results can be called into the same editor resulting in more streamlined workflow.[2] The code structure still includes mostly the same .f90 files although they are heavily modified due to continues development. Nevertheless the basic Rayleigh computations can be easily implemented by identifying

[1] For a detailed description of the source files and outputs of `CAMB` see the README file: https://CAMB.info/readme.html

[2] For a detailed documentation of the `CAMB` python wrapper see: https://CAMB.readthedocs.io/en/latest/

where the new version computes the visibility function and introducing the Rayleigh term as outlined in section 2.2.1.

3.2 Fisher forecasts and parameter estimation

The tested parameters are shown in table 1 with their fiducial value and step size for determining the numerical derivatives. The six ΛCDM parameters are taken from Planck Collaboration [11] and the three EDE from Hill et al. [17]. The step sizes were varied until a converging derivative with respect to the parameters was achieved. Here $\Omega_b h^2$ and $\Omega_c h^2$ are the physical densities of baryons and cold dark matter in the universe respectively.[3]

Parameter	Fiducial value	Step size
$\Omega_b h^2$	0.02237	$8 \cdot 10^{-6}$
$\Omega_c h^2$	0.120	$3 \cdot 10^{-5}$
$10^9 A_s$	2.099	0.01
n_s	0.9649	0.001
H_0 [km/s/Mpc]	67.3	0.001
τ	0.0544	$5 \cdot 10^{-4}$
$f_{\rm EDE}$	0.122	$1 \cdot 10^{-6}$
z_c	$10^{3.562}$	1
θ_i	2.83	$1 \cdot 10^{-4}$

Table 1: List of six ΛCDM [11] and three EDE parameters [17] used and their Fiducial value and step size when determining the derivative.

As the Raleigh auto RR and cross TR correlations cannot be calculated in the first modified version of `CAMB`, only single frequency Thomson+Rayleigh spectra are computed, they must be calculated indirectly. This is done by decomposing the computed spectra at different frequencies in terms of the Thomson C_ℓ^{TT} and Rayleigh C_ℓ^{RR} auto spectrum and the cross correlation C_ℓ^{TR} of the two modes. As there are three unknowns, a system of three equations is required to solve each term. To solve the system, the spectra are calculated at frequencies 0, 500 and 750 GHz and decomposed into:

$$\begin{cases} C_\ell^{0} \quad = C_\ell^{TT} \\ C_\ell^{500} = C_\ell^{TT} + 2C_l^{TR} + C_\ell^{RR} \\ C_\ell^{750} = C_\ell^{TT} + 2\left(\frac{750}{500}\right)^4 C_\ell^{TR} + \left(\frac{750}{500}\right)^8 C_\ell^{RR} \end{cases} \tag{20}$$

where the zero frequency is purely Thomson and thus equivalent to the temperature auto spectrum. The other frequency spectra do include Rayleigh so the total spectrum is decomposed into $(T+R)^2 = TT + 2TR + RR$. The 750 GHz spectrum is rescaled to the 500 GHz for proper normalization. The system can be rewritten into:

$$\begin{cases} C_\ell^{TT} = C_\ell^{0} \\ C_\ell^{TR} = \frac{1}{2\left(1-\left(\frac{500}{750}\right)^4\right)} \left[C_\ell^{500} - C_\ell^{0} - \left(\frac{500}{750}\right)^8 \left[C_\ell^{750} - C_\ell^{0}\right]\right] \\ C_\ell^{RR} = \frac{1}{\left(1-\left(\frac{750}{500}\right)^4\right)} \left[C_\ell^{500} - C_\ell^{0} - \left(\frac{500}{750}\right)^4 \left[C_\ell^{750} - C_\ell^{0}\right]\right] \end{cases} \tag{21}$$

3.3 Noise Modelling

The noise spectra curves in the cross elements of the covariance matrices (Eqs. (18) and (19)) are taken from the PICO (Probe of Inflation and Cosmic Origin) mission which is a proposed CMB mapping satellite

[3] The physical density is defined as $\Omega_i \equiv \epsilon_i/\epsilon_c$ with ϵ_i the energy density of the specific component and ϵ_c the critical energy density required for a spatially flat universe [1].

equipped with 21 frequency channels ranging from 21 to 799 GHz. This mission is expected to deepen our understanding of foreground contamination and its frequency channels offers the chance to better study Rayleigh scattering effects in the CMB [2]. Its Gaussian white noise in C_ℓ is [21]:

$$N_\ell^{TT'} = s^2 \exp\left(\ell(\ell+1)\,\frac{\theta_{FWHM}^2}{8\log 2}\right), \tag{22}$$

with s the total intensity instrumental noise in units of μK and θ_{FWHM} the full width at half maximum beam size in radians. The parameter noise values for the various PICO frequency channels are taken from [22].

4 Results

The detailed code modifications made to the python branch of `CAMB` are shown in the Appendix (8) and are used to obtain the following results.

4.1 Rayleigh effect on power spectra

With the modified code, a 500 GHz Rayleigh scattering enabled power spectrum was compared to a zero frequency Thomson primary spectrum for both lensed scalar TT and EE modes shown in Figure 2. This plot is similar to previous studies on Rayleigh effects [2], [3], [6] and confirms the working of the code. For a detailed analysis of the new `CAMB` version the fractional difference between the old and new

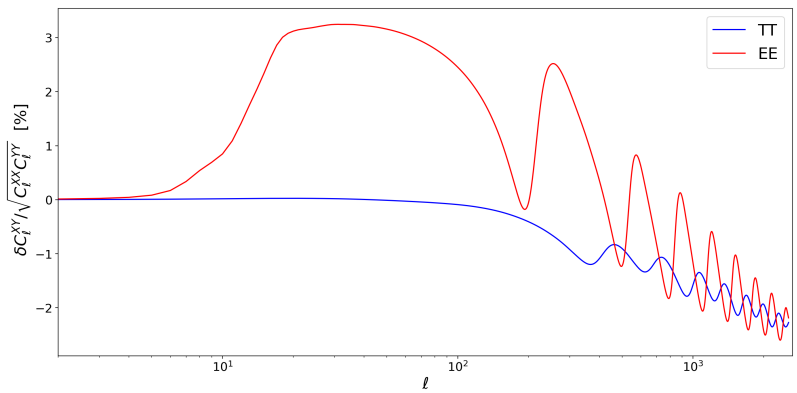

Figure 2: Fractional difference between the modified `CAMB` Thomson primary and 500 GHz Rayleigh power spectra for lensed scalar TT and EE.

Rayleigh code is shown in Figure 3. The sub-percentile differences displayed could however be caused by the general divergence between the Fortran and Python branch. To discern differences caused only by the Rayleigh implementation, the baseline Thomson primary fractional difference between the Fortran and Python branches was subtracted from this signal shown in Figure 4. Here the fractional differences are at a sub-percentile level at best at the highest ℓ.

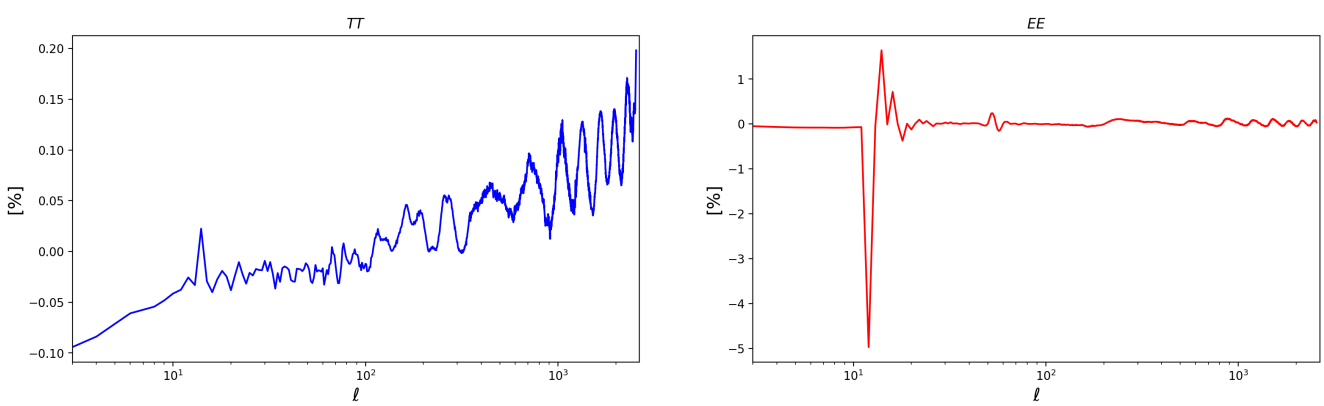

Figure 3: Fractional difference between the old Rayleigh branch and Rayleigh modified python branch of `CAMB` for both the lensed scalar TT and EE modes. Rayleigh signals at 500 GHz.

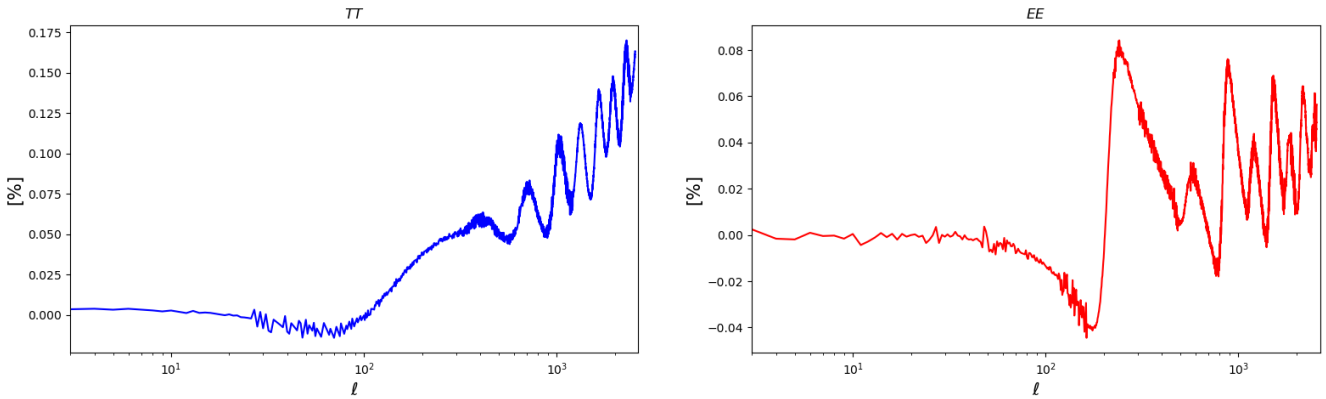

Figure 4: Fractional difference between the old Rayleigh branch and Rayleigh modified python branch of `CAMB` minus the fractional difference of the old and new `CAMB` Thomson primary for both the lensed scalar TT and EE modes. Rayleigh signals at 500 GHz.

4.2 Fisher forecasts and Early Dark Energy

The lensed Thomson and Rayleigh auto and cross correlation terms derived using equations (21) are shown in Figure 5 for 500 and 750 GHz from $\ell = 2$ to $\ell = 3000$. Additionally, in Figure 6 these terms are shown for 90 and 555 GHz and the accompanying PICO noise curves used to compute the EDE parameter forecast. When the noise curve is below the various terms it signifies the signal detectability is mostly limited by cosmic variance.

For the calculation of the Fisher information matrices the numerical derivatives with respect to the nine parameters are computed (see Eq. (15)) and are shown in Figures 7 and 8.

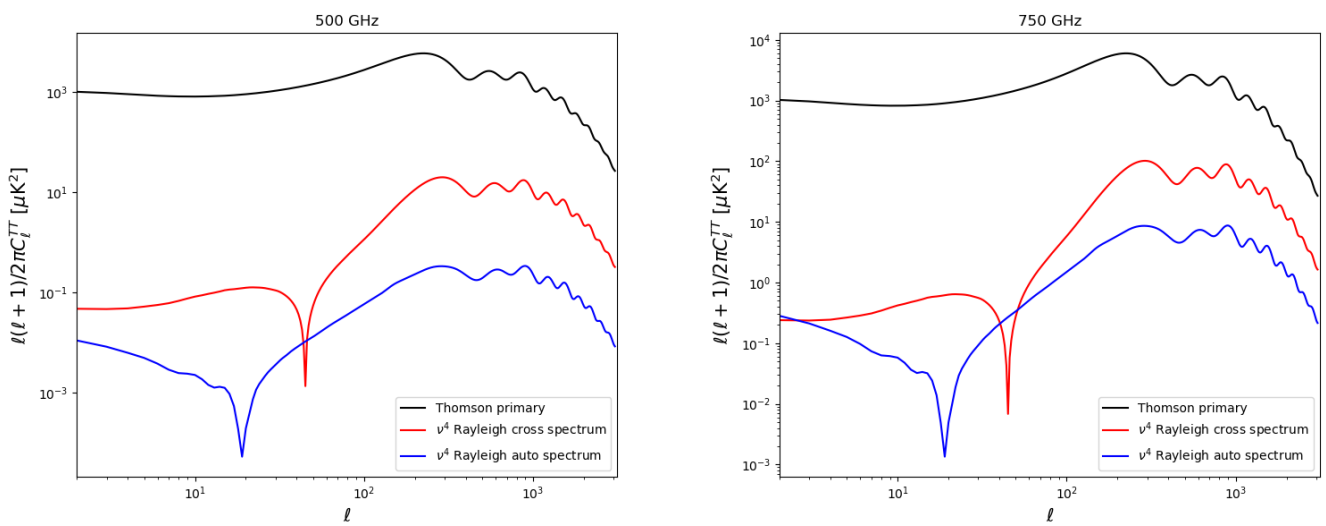

Figure 5: The lensed Thomson and Rayleigh (TT, TR and RR) terms derived from the expansion given in Eq. (21) for 500 and 750 GHz. Note the absolute values of Rayleigh TR and RR terms are given here where the downwards peak denotes a switch of sign.

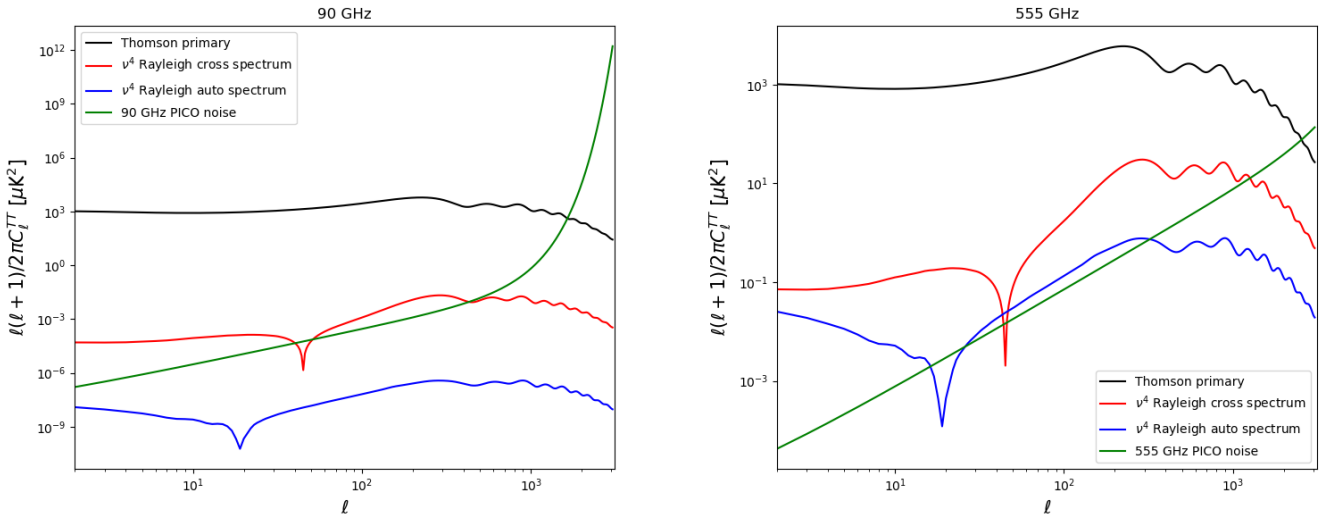

Figure 6: The lensed Thomson and Rayleigh terms (TT, TR and RR) derived from the expansion given in Eq. (21) for 90 and 555 GHz and the corresponding PICO noises.

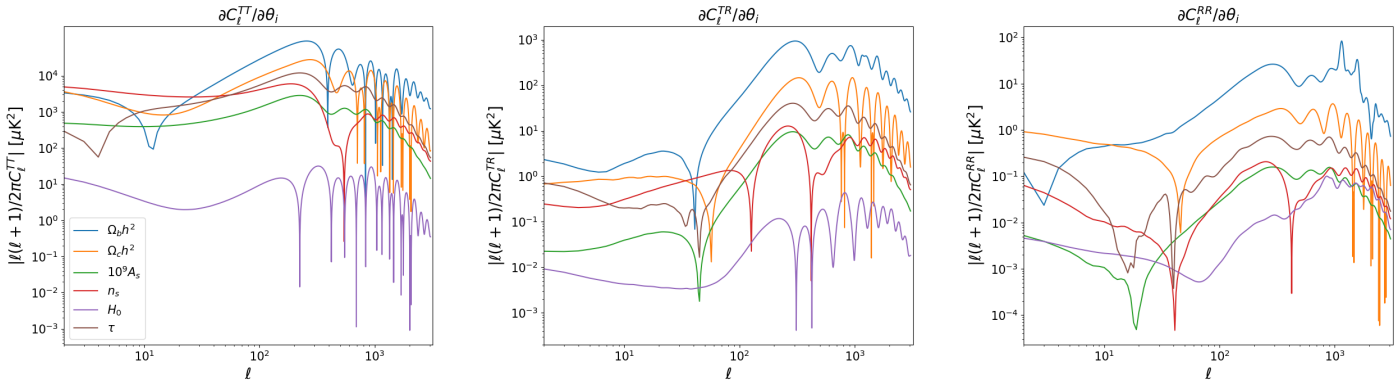

Figure 7: Absolute values of numerical derivatives $\partial C_\ell/\partial\theta_i$ of the six ΛCDM parameters used by Eq. (15) for the TT, TR and RR modes, scaled at 500 GHz.

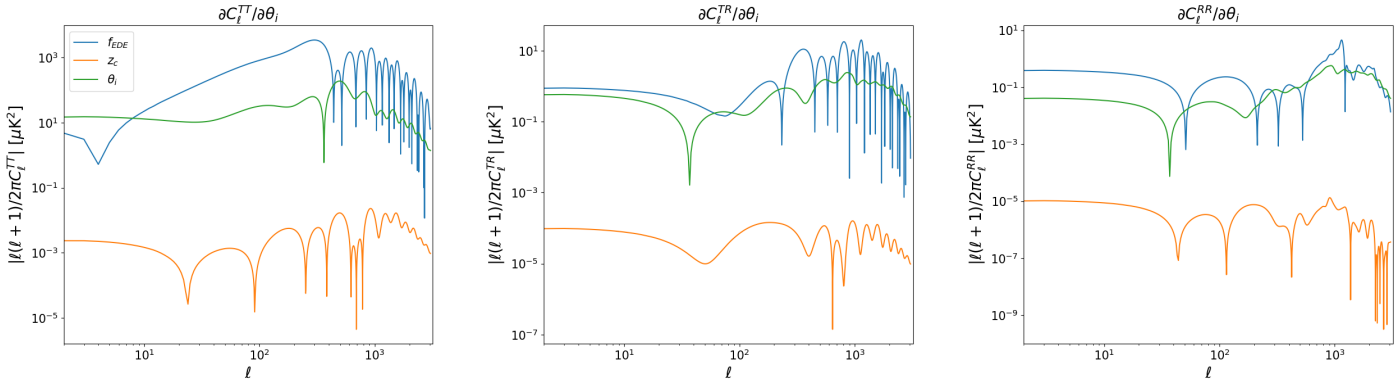

Figure 8: Absolute values of numerical derivatives $\partial C_\ell/\partial\theta_i$ of the three EDE parameters used by Eq. (15) for the TT, TR and RR modes, scaled at 500 GHz.

The Fisher matrices are obtained from the computed power spectra and converted to a parameter forecast using a Gaussian likelihood function. The forecast is shown in Figure 9 for the lensed Thomson and Rayleigh signals. The covariance matrices (Eqs. (18) and (19)) use a low frequency $\nu_1 = 90$ GHz map and PICO noise, as around this frequency the primary CMB is the best observable with the lowest noise, and a high frequency $\nu_2 = 555$ GHz map and PICO noise. Although the Rayleigh signal gets stronger at higher frequencies, the noise level also are greater. This results in the Rayleigh signal being best observable around 555 GHz

In our forecast, the diagonal graphs constitute the single parameter posteriors. The off-diagonal graphs go over every two parameter cross-correlation combination possible displaying the mutual parameter probability as ellipses. Here, circles represent no correlation between the two parameters as their probabilities are not interdependent. Meanwhile, narrow slanted ellipses constitute a strong (anti-)correlation between the two parameters as the value of one greatly narrows done the value of the other. Here an 45° slanted ellipse means a 100% correlation between the two parameters. The contours indicate a 1-σ (68%) confidence region. In Table 2 the 1-σ errors on the posteriors are listed for each parameter including the percentile improvements.

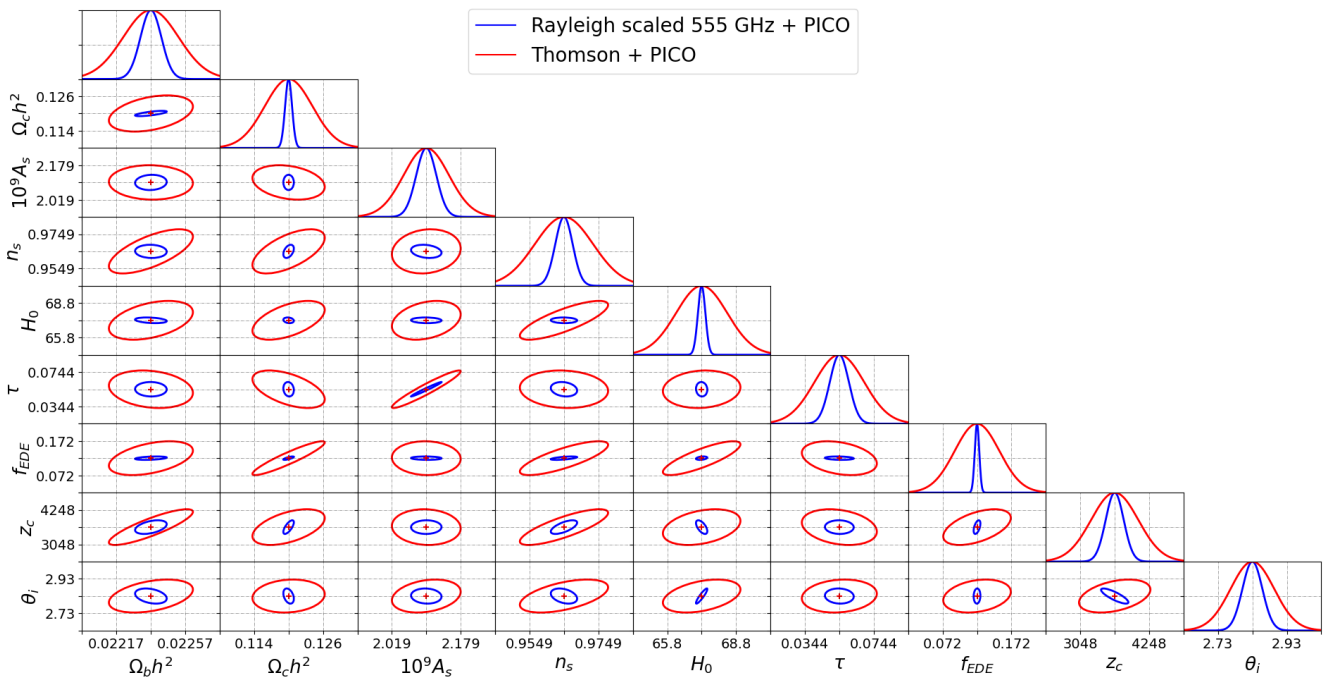

Figure 9: Fisher parameter forecast of the lensed Thomson primary signal and Rayleigh signal for a three parameter EDE extension to the ΛCDM model with six parameters including PICO noise. The red and blue contours show a 1σ confidence region. Fiducial values used are shown in Table 1. The covariance matrices used for the Rayleigh and Thomson forecasts are Eqs. (18) and (19) respectively with $\nu_1 = 90$GHz and $\nu_2 = 555$GHz.

Parameter	PICO Thomson only	PICO with Rayleigh	Improvement [%]
$\Omega_b h^2$	$1.61 \cdot 10^{-4}$	$6.06 \cdot 10^{-5}$	62.3
$\Omega_c h^2$	$4.15 \cdot 10^{-3}$	$6.04 \cdot 10^{-4}$	85.5
$10^9 A_s$	$5.27 \cdot 10^{-2}$	$2.33 \cdot 10^{-2}$	55.7
n_s	$8.45 \cdot 10^{-3}$	$2.52 \cdot 10^{-3}$	70.1
H_0 [km/s/Mpc]	1.11	$1.63 \cdot 10^{-1}$	85.4
τ	$1.44 \cdot 10^{-2}$	$5.52 \cdot 10^{-3}$	61.6
$f_{\rm EDE}$	$3.24 \cdot 10^{-2}$	$3.24 \cdot 10^{-3}$	90.0
z_c	$4.10 \cdot 10^{2}$	$1.57 \cdot 10^{2}$	61.8
θ_i	$6.31 \cdot 10^{-2}$	$2.89 \cdot 10^{-2}$	54.2

Table 2: List of 1-σ errors on parameter posteriors for the Thomson and Raleigh Fisher forecast in Figure 9 including percentile improvements.

5 Discussion

When analyzing the Rayleigh scattering implementation into the Python branch several things are noticed. First in Fig. 3, the Fortran and Python branches of `CAMB` output a notably different EE spectrum in comparison to the TT spectrum with a spike around $\ell \sim 10$. This is caused by the effect of Rayleigh scattering on EE having a large derivative at these same multipoles (see Fig. 2). Thus any offset would lead to large difference between the two branches. Previous forecasts using the Rayleigh E modes calculated using the Fortran branch of `CAMB` are therefore expected to slightly benefit from the Rayleigh implementation into the Python branch.

Furthermore, the approximation of the Rayleigh auto and cross spectra shown in Fig. 5 does not completely correspond with previous studies using code computing them directly [2], [3]. Especially at low ℓ does the Rayleigh auto (RR) spectrum differ as no sign change and no increase of the signal at lower ℓ are present in the other studies. At these low multipoles the spectrum should be roughly one order of magnitude smaller. This causes a conflict when incorporating noise as seen in Fig. 6 for the 555 GHz RR spectrum. At low ℓ the signal is only limited by cosmic variance while the noise curve decreases suggesting the Rayleigh auto spectrum is best detectable at these multipoles. This contradicts previous studies where the spectra should be more affected by foregrounds and instrumental noise at large angular scales [2]. Whether the approximation or the old `CAMB` version is inaccurate was not determined, although the Fisher forecasts should not change significantly as only few multipoles are affected. At high ℓ the auto and cross terms are approximated reasonably well showing clear acoustic oscillations. Furthermore, in Fig. 6 the Thomson primary is limited only by noise above $\ell \sim 1500$ for 90 GHz and $\ell \sim 2500$ at 555 GHz. Meanwhile at 555 GHz, the Rayleigh TR mode is only affected by noise at $\ell \sim 45$ and above $\ell \sim 1000$, while for RR noise contributes significantly at all multipoles except lower ℓ's. At 90 GHz, noise dominates the RR spectrum completely but is minor for TR at low to middle ℓ range, though still dominant over the acoustic oscillations. Thus, the TR spectrum is the greater contributor of Rayleigh effects to the Fisher information matrix when considering noise. Additionally, the numerical spectrum derivatives in Fig. 7 and 8 are smooth for the TT and TR spectra with respect to all parameters with oscillations at high ℓ. These come from the acoustic oscillations in the C_ℓ's. However the RR spectrum is not smooth for most parameters. Smoothness is expected as accurately computed terms should be continuous in the first derivative with respect to all parameters. Again, this irregularity indicates that the RR spectrum approximation is not fully correct.

Looking at the Fisher forecasts in Fig. 9 the parameter confidence contours are significantly smaller when including Rayleigh effects. In Table 2, the Rayleigh parameter errors improve from 54 to 90 % with respect to the Thomson forecast, constraining the parameters errors substantially. However, stochastically mode counting two signals (Thomson and Rayleigh) should only, at best, give a $1/\sqrt{2}$ reduction (29.3% improvement) in the parameter errors if both modes are uncorrelated, which they are not. This significant improvement in the parameter errors, in particular for $\Omega_c h^2$, H_0 and $f_{\rm EDE}$, are thus not expected and hints to a mistake somewhere in the calculations. The missing $C_\ell^{RR}(\nu_1 \times \nu_2)$ term in the covariance matrices correlating the low and high frequency maps could be the possible culprit. Additionally, only the temperature signal was used which could result in a initial poor forecast but constraining tightly when including Rayleigh. This performance is likely to decrease when also including polarization.

Moreover, the individual likelihood regions are reasonable as the found ΛCDM parameter intervals are slightly worse compared to other studies [2], [6], being roughly one order of magnitude bigger. This is caused by excluding polarization effects in the forecasts causing overall worse constraining power. Moreover, the expected high correlation between τ and $10^9 A_s$ is observed, being a key feature in ΛCDM forecasts. But despite that, checking the correctness of the other parameter correlations is harder as no independent method was readily available to verify the results.

6 Conclusions

The Rayleigh TT and EE auto correlation spectra implementation to the Python branch of `CAMB` produced accurate results for both spectra compared to the Fortran Rayleigh branch. For both spectra the differences are greatest at higher ℓ values although still far below and around sub-percentile level making this code usable for modelling single-frequency Rayleigh effects in the CMB. Multi-frequency and cross-correlation spectra calculations are not yet coded into this version but will be included in future development of the code. For the remaining calculations an indirect derivation of the Rayleigh auto and cross spectra was used to obtain the results. This approximation gave an accurate Rayleigh cross spectrum C_ℓ^{TR}. However, the Rayleigh auto spectrum C_ℓ^{RR} deviated at low ℓ having a sign switch and being an order of magnitude too large compared to previous studies. At higher ℓ however the spectrum is accurate. The numerical derivatives with respect to the three EDE and six ΛCDM parameters, used to produce the Fisher information matrix, are smooth for C_ℓ^{TT} and C_ℓ^{TR} except C_ℓ^{RR}. Again indicating the RR spectrum is not fully accurate leading to PICO noise curves suggesting RR is mostly cosmic variance limited at low ℓ. However, the possibility exist the old `CAMB` determines the Rayleigh terms incorrectly although this was not further studied.

The Fisher forecasts of a three parameter EDE extension to a six parameter ΛCDM model resulted in the Rayleigh signal to produce parameter likelihoods improved by 54 to 90 % compared to the Thomson primary forecast. In particular $\Omega_c h^2$, H_0 and $f_{\rm EDE}$ are heavily constrained. This significant improvement in the constraining power is surprising based on mode counting estimates. The approximation of cross-correlating a low and high frequency map in the covariance matrices and only using the temperature signal are the possible sources. Nevertheless, the individual parameter intervals are reasonable, being an order of magnitude greater than previous studies caused by excluding the polarization signal in the forecast. Independently verifying the results was not done but shall be continued in upcoming studies. Here, further development in including multi-frequency correlated Rayleigh signals into `CAMB` could obtain more reasonable forecasts and accurately demonstrate the constraining power of Rayleigh on EDE models. With the prospect of a first Rayleigh detection in the upcoming decade, further developments in modeling Rayleigh scattering brings us one step closer to fully understanding its effects on cosmological models, giving us new avenues of obtaining information on our early universe.

7 References

[1] B. Ryden, *Introduction to Cosmology*, 2nd ed. Cambridge University Press, 2017, ISBN: 9781107154834.

[2] B. Beringue, P. D. Meerburg, J. Meyers, and N. Battaglia, "Cosmology with rayleigh scattering of the cosmic microwave background," *Journal of Cosmology and Astroparticle Physics*, vol. 2021, no. 01, pp. 060–060, Jan. 2021. DOI: 10.1088/1475-7516/2021/01/060.

[3] A. Lewis, "Rayleigh scattering: Blue sky thinking for future cmb observations," *Journal of Cosmology and Astroparticle Physics*, vol. 2013, no. 08, p. 053, Aug. 2013. DOI: 10.1088/1475-7516/2013/08/053.

[4] Y. Zhu, B. Beringue, S. K. Choi, N. Battaglia, P. D. Meerburg, and J. Meyers, "Estimating the impact of foregrounds on the future detection of rayleigh scattering," *Journal of Cosmology and Astroparticle Physics*, vol. 2022, no. 09, p. 048, Sep. 2022. DOI: 10.1088/1475-7516/2022/09/048.

[5] R. L. Workman *et al.*, "25. Cosmological parameters," in *Review of Particle Physics*, vol. 2022, Aug. 2022, pp. 467–475. DOI: 10.1093/ptep/ptac097.

[6] E. Alipour, K. Sigurdson, and C. M. Hirata, "Effects of rayleigh scattering on the CMB and cosmic structure," *Phys. Rev. D*, vol. 91, p. 083 520, 8 Apr. 2015. DOI: 10.1103/PhysRevD.91.083520.

[7] W. R. Coulton, B. Beringue, and P. D. Meerburg, "Primordial information content of rayleigh anisotropies," *Physical Review D*, vol. 103, no. 4, Feb. 2021. DOI: 10.1103/physrevd.103.043501.

[8] D. Samtleben, S. Staggs, and B. Winstein, "The cosmic microwave background for pedestrians: A review for particle and nuclear physicists," *Annual Review of Nuclear and Particle Science*, vol. 57, no. 1, pp. 245–283, Nov. 2007. DOI: 10.1146/annurev.nucl.54.070103.181232.

[9] R. L. Workman *et al.*, "23. Inflation," in *Review of Particle Physics*, vol. 2022, Aug. 2022, pp. 443–458. DOI: 10.1093/ptep/ptac097.

[10] S. Dodelson and F. Schmidt, *Modern Cosmology*, 2nd ed. Elsevier Science, 2020, ISBN: 9780128159484.

[11] Planck Collaboration, N. Aghanim, Y. Akrami, *et al.*, "Planck 2018 results - VI. cosmological parameters," *Astronomy & Astrophysics*, vol. 641, A6, 2020. DOI: 10.1051/0004-6361/201833910.

[12] B. Beringue, "Rayleigh scattering of the Cosmic Microwave Background: Towards a first detection with the next generation of surveys," Ph.D. dissertation, Cambridge U., DAMTP, Oct. 2021. DOI: 10.17863/CAM.92680.

[13] R. L. Workman *et al.*, "29. Cosmic Microwave Background," in *Review of Particle Physics*, vol. 2022, Aug. 2022, pp. 509–519. DOI: 10.1093/ptep/ptac097.

[14] A. G. Riess, W. Yuan, L. M. Macri, *et al.*, "A comprehensive measurement of the local value of the hubble constant with 1 km s^{-1} mpc^{-1} uncertainty from the hubble space telescope and the SH0ES team," *The Astrophysical Journal Letters*, vol. 934, no. 1, p. L7, Jul. 2022. DOI: 10.3847/2041-8213/ac5c5b.

[15] M. Kamionkowski and A. G. Riess, *The hubble tension and early dark energy*, 2022. arXiv: 2211.04492.

[16] V. Poulin, T. L. Smith, T. Karwal, and M. Kamionkowski, "Early dark energy can resolve the hubble tension," *Physical Review Letters*, vol. 122, no. 22, Jun. 2019. DOI: 10.1103/physrevlett.122.221301.

[17] J. C. Hill, E. McDonough, M. W. Toomey, and S. Alexander, "Early dark energy does not restore cosmological concordance," *Physical Review D*, vol. 102, no. 4, Aug. 2020. DOI: 10.1103/physrevd.102.043507.

[18] V. Poulin, T. L. Smith, and T. Karwal, *The ups and downs of early dark energy solutions to the hubble tension: A review of models, hints and constraints circa 2023*, 2023. arXiv: 2302.09032.

[19] L. Verde, "Statistical methods in cosmology," in *Lectures on Cosmology*, Springer Berlin Heidelberg, 2010, pp. 147–177. DOI: 10.1007/978-3-642-10598-2_4.

[20] A. Lewis, A. Challinor, and A. Lasenby, "Efficient computation of cosmic microwave background anisotropies in closed friedmann-robertson-walker models," *The Astrophysical Journal*, vol. 538, no. 2, pp. 473–476, Aug. 2000. DOI: 10.1086/309179.

[21] W. L. K. Wu, J. Errard, C. Dvorkin, *et al.*, "A GUIDE TO DESIGNING FUTURE GROUND-BASED COSMIC MICROWAVE BACKGROUND EXPERIMENTS," *The Astrophysical Journal*, vol. 788, no. 2, p. 138, Jun. 2014. DOI: 10.1088/0004-637x/788/2/138.

[22] S. Hanany, M. Alvarez, E. Artis, *et al.*, *Pico: Probe of inflation and cosmic origins*, 2019. arXiv: 1902.10541 [astro-ph.IM].

8 Appendix: Code modifications

To classes.f90 a function and subroutine were added giving the functions used in results.f90 the right class type.

```
    procedure :: x_rayleigh_eff => TRecombinationModel_x_rayleigh_eff
    procedure :: xrayleigh_eff => TRecombinationModel_xrayleigh_eff


    function TRecombinationModel_xrayleigh_eff(this,a)
    class(TRecombinationModel) :: this
    real(dl), intent(in) :: a
    real(dl) TRecombinationModel_xrayleigh_eff
    call MpiStop('TRecombinationModel_xrayleigh not implemented')
    TRecombinationModel_xrayleigh_eff=0

    end function TRecombinationModel_xrayleigh_eff

    subroutine TRecombinationModel_x_rayleigh_eff(this,a, xrayleigh_eff_var)
    class(TRecombinationModel) :: this
    real(dl), intent(in) :: a
    real(dl), intent(out) :: xrayleigh_eff_var
    xrayleigh_eff_var = this%xrayleigh_eff(a)

    end subroutine TRecombinationModel_x_rayleigh_eff
```

In recfast.f90, containing the recombination calculations, the function `TRecfast_xrayleigh_eff` was added that calculates the recombination fraction

```
    ! In module recombination
    real(dl), private :: xrayrec(Nz), dxrayrec(Nz)

    procedure :: xrayleigh_eff => TRecfast_xrayleigh_eff

    function TRecfast_xrayleigh_eff(this,a)
    class(TRecfast) :: this
    real(dl), intent(in) :: a
    real(dl) zst,z,az,bz,TRecfast_xrayleigh_eff
    integer ilo,ihi

    z=1/a-1
    associate(Calc => this%Calc)
        if (z.ge.Calc%zrec(1)) then
            TRecfast_xrayleigh_eff=Calc%xrayrec(1)
        else
            if (z.le.Calc%zrec(nz)) then
                TRecfast_xrayleigh_eff=Calc%xrayrec(nz)
            else
                zst=(zinitial-z)/delta_z
                ihi= int(zst)
                ilo = ihi+1
                az=zst - ihi
                bz=1-az
                TRecfast_xrayleigh_eff=az*Calc%xrayrec(ilo)+bz*Calc%xrayrec(ihi)+ &
                    ((az**3-az)*Calc%dxrayrec(ilo)+(bz**3-bz)*Calc%dxrayrec(ihi))/6._dl
            endif
        endif
    end associate
    end function TRecfast_xrayleigh_eff

     ! In subroutine TRecfast_init
     Calc%xrayrec(i) = 1._dl - x_H + 0.1_dl*(1._dl - x_He)*Calc%fHe
```

```

    call spline_def(Calc%zrec,Calc%xrayrec,nz,Calc%dxrayrec)
```

Lastly, the functions and subroutines defined earlier are applied to results.f90 by adding the Raleigh scattering term to the visibility function as outlined in section 2.2.1.

```
    ! In subroutine Thermo_Init
    real(dl), parameter :: nu_eff = 3101692._dl

    real(dl), allocatable :: xrayleigh_eff_a(:)

    allocate(taus(nthermo), xe_a(nthermo), xrayleigh_eff_a(nthermo))

    call CP%Recomb%x_rayleigh_eff(a0, xrayleigh_eff_a(1))

    this%dotmu(1)=(this%xe(1)+ xrayleigh_eff_a(1) * (500._dl / (a0*nu_eff))**4 )*State%
    akthom/a0**2

    call CP%Recomb%x_rayleigh_eff(this%scaleFactor(i), xrayleigh_eff_a(i))

    this%dotmu(i)=(this%xe(i)+ xrayleigh_eff_a(i) * ((500._dl / nu_eff)**4)/a2**2)*State
    %akthom/a2
```